The Astrophysical Journal, 828:107 (11pp), 2016 September 10 doi:10.3847/0004-637X/828/2/107

SPECTROSCOPIC MEASUREMENTS OF THE FAR-ULTRAVIOLET DUST ATTENUATION CURVE AT $z \sim 3$*

Naveen A. Reddy[1,6], Charles C. Steidel[2], Max Pettini[3], and Milan Bogosavljević[4,5]
[1] Department of Physics and Astronomy, University of California, Riverside, 900 University Avenue, Riverside, CA 92521, USA
[2] Department of Astronomy, California Institute of Technology, MS 105–24, Pasadena, CA 91125, USA
[3] Institute of Astronomy, Madingley Road, Cambridge CB3 OHA, UK
[4] Astronomical Observatory, Belgrade, Volgina 7, 11060 Belgrade, Serbia
[5] New York University Abu Dhabi, P.O. Box 129188, Abu Dhabi, UAE
Received 2015 December 7; revised 2016 May 10; accepted 2016 May 23; published 2016 September 8

ABSTRACT

We present the first spectroscopic measurements of the shape of the far-ultraviolet (far-UV; $\lambda = 950$–1500 Å) dust attenuation curve at high redshift ($z \sim 3$). Our analysis employs rest-frame UV spectra of 933 galaxies at $z \sim 3$, 121 of which have very deep spectroscopic observations ($\gtrsim$7 hr) at $\lambda = 850$–1300 Å, with the Low Resolution Imaging Spectrograph on the Keck Telescope. By using an iterative approach in which we calculate the ratios of composite spectra in different bins of continuum color excess, $E(B-V)$, we derive a dust curve that implies a lower attenuation in the far-UV for a given $E(B-V)$ than those obtained with standard attenuation curves. We demonstrate that the UV composite spectra of $z \sim 3$ galaxies can be modeled well by assuming our new attenuation curve, a high covering fraction of H I, and absorption from the Lyman–Werner bands of H_2 with a small ($\lesssim$20%) covering fraction. The low covering fraction of H_2 relative to that of the H I and dust suggests that most of the dust in the ISM of typical galaxies at $z \sim 3$ is unrelated to the catalysis of H_2, and is associated with other phases of the ISM (i.e., the ionized and neutral gas). The far-UV dust curve implies a factor of $\approx$2 lower dust attenuation of Lyman continuum (ionizing) photons relative to those inferred from the most commonly assumed attenuation curves for L^* galaxies at $z \sim 3$. Our results may be utilized to assess the degree to which ionizing photons are attenuated in H II regions or, more generally, in the ionized or low column density (N(H I) $\lesssim 10^{17.2}$ cm^{-2}) neutral ISM of high-redshift galaxies.

Key words: dark ages, reionization, first stars – dust, extinction – galaxies: evolution – galaxies: formation – galaxies: high-redshift – galaxies: ISM

1. INTRODUCTION

The dust attenuation curve is a principal tool for inferring the absorption and scattering properties of interstellar dust grains, the spatial distribution of that dust relative to stars, and the intrinsic stellar populations of galaxies. Observations of nearby galaxies have yielded detailed information on both the normalization and shape of the dust curve (e.g., Calzetti et al. 1994, 2000; Johnson et al. 2007; Wild et al. 2011). In contrast, our knowledge of the dust curve (and how the curve varies) at high redshift has only recently improved with large multi-wavelength and spectroscopic surveys (e.g., Noll et al. 2009; Buat et al. 2011, 2012; Kriek & Conroy 2013; Reddy et al. 2015; Salmon et al. 2015; Scoville et al. 2015; Zeimann et al. 2015).

Despite these advances, the detailed shape of the attenuation curve at far-ultraviolet (far-UV) wavelengths, in particular at $\lambda \lesssim 1250$ Å, remains largely unconstrained at high redshift. Establishing the shape of this curve at these wavelengths is imperative for several reasons. First, dust obscuration of starlight reaches its maximum in the far-UV, such that even small differences in the continuum color excess, $E(B-V)$, may lead to large variations in the inferred attenuation of far-UV light. Hence, inferences of the intrinsic formation rate of the very massive stars that dominate the far-UV require knowledge of the shape of the dust curve at these wavelengths. Second, the translation between reddening and far-UV color depends on the shape of the far-UV attenuation curve. Therefore, different shapes of the far-UV curve will result in different color criteria to select galaxies at intermediate redshifts ($1.5 \lesssim z \lesssim 4.0$) where the Ly$\alpha$ forest is sufficiently thin and where the selection may include photometric bands that lie blueward of Lyα. Stated another way, fixed far-UV color selection criteria will select galaxies at slightly different redshifts depending on the shape of the UV dust attenuation curve, and may affect the inferred selection volumes that are necessary for computing UV luminosity functions (e.g., Steidel & Hamilton 1993; Steidel et al. 2003; Adelberger et al. 2004; Sawicki & Thompson 2006; Reddy et al. 2008). Third, the utility of the Lyα emission line as a probe of the physical conditions (e.g., dust/gas distribution, gas kinematics) in high-redshift galaxies requires some knowledge of dust grain properties and the distribution of the dust in the ISM (e.g., Meier & Terlevich 1981; Calzetti & Kinney 1992; Charlot & Fall 1993; Giavalisco et al. 1996; Verhamme et al. 2008; Scarlata et al. 2009; Finkelstein et al. 2011; Hayes et al. 2011; Atek et al. 2014), both of which are reflected in the shape of the attenuation curve. Fourth, there has been renewed attention in the modeling of massive stars (Eldridge & Stanway 2009; Brott et al. 2011; Levesque et al. 2012; Leitherer et al. 2014) given evidence of rest-optical line ratios (Steidel et al. 2014; Shapley et al. 2015) and UV spectral features of $z \sim 2$–3 galaxies (Steidel et al. 2016) that cannot be modeled simultaneously with standard stellar population synthesis models. The modeling of the far-UV continuum of high-redshift galaxies is sensitive to the assumed dust attenuation curve. Lastly, knowledge of the attenuation curve at or near the Lyman

* Based on data obtained at the W.M. Keck Observatory, which is operated as a scientific partnership among the California Institute of Technology, the University of California, and NASA, and was made possible by the generous financial support of the W.M. Keck Foundation.
[6] Alfred P. Sloan Research Fellow.

break is needed to deduce the effect of dust obscuration on the depletion of hydrogen-ionizing photons, a potentially important ingredient in assessing the contribution of galaxies to reionization and translating recombination line luminosities to star formation rates.

Given the relevance of the far-UV shape of the dust attenuation curve, we sought to use the existing large spectroscopic samples of Lyman Break galaxies (LBGs) at $z \sim 3$ to provide the first direct spectroscopic constraints on the shape of this curve at high redshift. In Section 2 we discuss the sample of galaxies and the procedure to construct far-UV spectral composites. The calculation of the far-UV dust attenuation curve is presented in Section 3. In Section 4 we assess whether the dust curve can be used in conjunction with spectral models to reproduce the composite UV spectra. The implications of our results are discussed in Section 5, and we summarize in Section 6. All wavelengths are in vacuum. All magnitudes are expressed in the AB system. We adopt a cosmology with $H_0 = 70$ km s^{-1} Mpc^{-1}, $\Omega_\Lambda = 0.7$, and $\Omega_m = 0.3$.

2. SAMPLE SELECTION AND REST-FRAME UV SPECTROSCOPY

2.1. Lyman Break Selected Samples at $z \sim 3$

The galaxies used in our analysis were drawn from the Lyman Break selected and spectroscopically confirmed sample described in Steidel et al. (2003). In brief, these galaxies were selected as z $\sim$ 3 candidates based on their rest-frame UV ($U_n - G$ and $G - \mathcal{R}_s$) colors as measured from ground-based imaging of 17 fields. Of the 2347 $\mathcal{R}_s \leqslant 25.5$ LBG candidates, 1293 were observed spectroscopically with the original single channel configuration of the Low Resolution Imaging Spectrograph (LRIS; Oke et al. 1995) on the Keck telescopes, with a typical integration time of $\simeq$1.5 hr. The spectroscopy was accomplished using the 300 lines mm^{-1} grating blazed at 5000 Å giving a typical observed wavelength coverage of $\lambda_{obs} \approx$ 4000–7000 Å with 2.47 Å pix^{-1} dispersion. The spectral resolution, including the effects of seeing, is $\approx$7.5 Å in the observed frame. Redshifts were determined from either interstellar absorption lines at λ_{rest} = 1200–1700 Å, or from Lyα emission. In some cases, the detection of a single emission line with a continuum break shortward of that line was used to assign a secure redshift. Our sample includes only those galaxies with secure emission and/or absorption line redshifts that were vetted by at least two people and published in Steidel et al. (2003). Further details of the photometry, candidate selection, follow-up spectroscopy, and data reduction are provided in Steidel et al. (2003).

Subsequent deep ($\simeq$7–10 hr) spectroscopy was obtained for a sample of 121 $2.7 < z < 3.6$ galaxies with existing spectroscopic redshifts from the Steidel et al. (2003, 2004) samples, with the aim of obtaining very sensitive observations of the Lyman continuum (LyC) emission blueward of the Lyman limit ($\lambda < 912$ Å)—we refer to the set of objects with deeper spectroscopy as the "LyC sample." This spectroscopy was obtained using the blue channel of the upgraded double spectrograph mode of LRIS (Steidel et al. 2004), which presents a factor of 3–4 improvement in throughput at 4000 Å relative to the red-side channel. The new configuration of LRIS includes an atmospheric dispersion corrector that eliminates wavelength dependent slit losses. The deep spectroscopic observations were obtained using the d500 dichroic with the 400 lines mm^{-1} grism blazed at 3400 Å, yielding a (binned) dispersion of 2.18 Å pix^{-1}. Including the effect of seeing, the typical observed-frame resolution is $\approx$7 Å for the blue channel spectra. Redshifts were determined using the same procedure as for the Steidel et al. (2003) sample (see above). The depth of the spectroscopic observations for the LyC sample allowed us to assign absorption line redshifts for $\approx$92% of the objects. The 121 galaxies of the LyC sample excludes all objects ($\approx$5% of the sample) where the deep spectra indicated a blend between the target LBG and a foreground galaxy. Details of the data reduction and spectroscopy are provided in C. C. Steidel et al. (2016, in preparation).

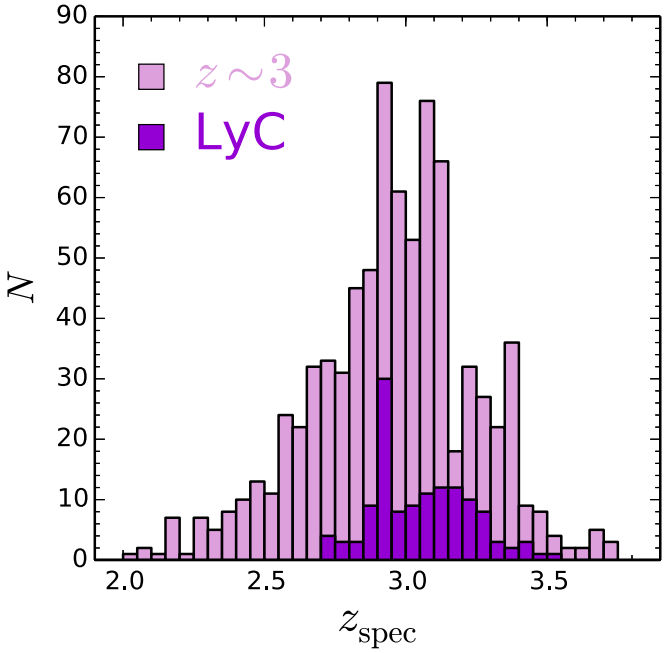

Figure 1. Redshift distribution of 933 star-forming galaxies in our sample, consisting of objects drawn from Steidel et al. (2003) (*light region*) and the deep LyC survey (*dark region*). The excess number of redshifts (by a factor of $\gtrsim$3) in the range $2.90 < z < 2.95$ relative to adjacent redshift bins is due to an over-density of galaxies at $z \simeq 2.925$ in the Westphal field.

We further excluded active galactic nuclei (AGN) from the samples based on the presence of strong UV emission lines (e.g., Lyα and C IV). The AGN fraction in the $z \sim 3$ sample (to the magnitude limit of $\mathcal{R}_s = 25.5$) based on strong UV emission lines is $\approx$3% (e.g., Steidel et al. 2003; Reddy et al. 2008). We did not have the requisite multi-wavelength (infrared, X-ray) data for the majority of the fields to identify AGN using other methods. However, we note that optically identified AGN in UV-selected samples comprise $\approx$70% of AGN identified either from X-ray emission or from a mid-infrared excess (see Reddy et al. 2006), and we do not see evidence of AGN either in the remaining individual spectra or in the composite spectra.

Two important advantages of the $z \sim 3$ sample that facilitate spectroscopy in the far-UV region are the lower sky background in the observed optical relative to the near-infrared, and the fact that the Lyα forest is still relatively thin at these redshifts, allowing for the transmission of sufficient flux blueward of Lyα. Figure 1 shows the spectroscopic redshift distribution of our final sample, which includes 933 galaxies.

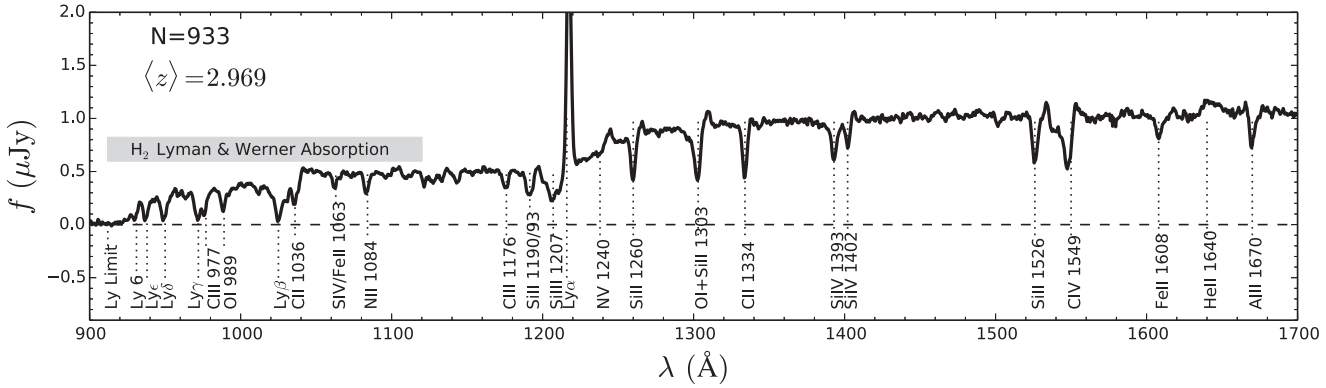

Figure 2. Composite spectrum of 933 galaxies at $z \sim 3$, with several of the most prominent stellar photospheric and interstellar absorption lines indicated. The far-UV range $\lambda = 912$–1120 Å is dominated by unresolved absorption from the Lyman and Werner bands of molecular hydrogen (H_2). The composite has been normalized by the median flux density in the range $\lambda = 1400$–1500 Å.

2.2. Composite Spectra

Throughout our analysis, we employed composite spectra which were computed by combining the individual spectra of galaxies. We first made separate composites of the galaxies in the $z \sim 3$ LBG and LyC samples, and then combined the two resulting composites to obtain a final composite. This procedure allows us to take advantage of the greater spectroscopic depth of the LyC objects in the far-UV range $\lambda_{\rm rest} = 912$–1150 Å.

For each galaxy in the $z \sim 3$ LBG sample, we determined the redshift using either emission (e.g., Lyα) and/or interstellar absorption lines. As these features are typically either redshifted (in the case of emission) or blueshifted (in the case of absorption) due to bulk flows of gas, we computed a systemic redshift from the emission and/or absorption line redshifts using the relations in Steidel et al. (2010). We then shifted each galaxy's spectrum into the rest frame using the systemic redshift, and interpolated the spectrum to a grid with a wavelength spacing of $\delta\lambda = 0.5$ Å. The error spectrum for each galaxy was shifted and interpolated accordingly, and then multiplied by $\sqrt{2}$ to account for wavelength resampling from the original dispersion of the reduced spectra of 1 Å pix^{-1}. Each spectrum was scaled according to the median flux density in the range $\lambda = 1400$–1500 Å. The individual galaxy spectra were then averaged, rejecting the upper and lower three flux density values in each $\delta\lambda$ interval.

The LyC composite was constructed using a similar procedure, with two exceptions. First, we did not scale the LyC spectra as the spectroscopic setup (with the d500 dichroic) precluded coverage of $\lambda = 1400$–1500 Å within the blue channel of LRIS. Second, we combined the LyC spectra using a weighted average, where the weights are $w(\lambda) = 1/\sigma^2(\lambda)$, where $\sigma(\lambda)$ is the error spectrum. We still rejected the upper and lower three weighted flux density values in each $\delta\lambda$ interval.

The LyC composite was scaled to have the same median flux density in the range $\lambda = 1100$–1150 Å as that of the $z \sim 3$ LBG composite. The final composite results from combining the scaled LyC composite at $\lambda \leqslant 1150$ Å and the $z \sim 3$ LBG composite at $\lambda > 1150$ Å. We confirmed that this combination does not introduce a systematic bias in the level of the stellar continuum of the composite below and above $\lambda = 1150$ Å. The mean redshifts of the objects contributing to the composite spectrum at the blue (912 Å) and red (1600 Å) ends of the composite spectrum are $\langle z \rangle = 3.058$ and 2.940, respectively. Given this small difference in redshift, corresponding to $\delta t \approx 92$ Myr, we assumed that the LBG spectral properties do not vary over this short time interval. The final composite is shown in Figure 2, normalized such that the median flux density in the range $\lambda = 1400$–1500 Å is unity. The error spectrum corresponding to the composite was computed as the weighted combination of the error spectra of the individual objects contributing to the composite. The error in the mean flux of the composite is <0.1 μJy for the scaling and full wavelength range shown in Figure 2.

3. FAR-UV ATTENUATION CURVE

The method of computing the far-UV attenuation curve, $k(\lambda)$, is based on taking the ratios of composite spectra in bins of $E(B-V)$. The attenuation curve is defined as

$$k(\lambda) \equiv \frac{-2.5}{E(B-V)_{i+1} - E(B-V)_i} \log\left[\frac{f_{i+1}(\lambda)}{f_i(\lambda)}\right], \quad (1)$$

where $f_i(\lambda)$ and $E(B-V)_i$ refer to the average flux density and average $E(B-V)$, respectively, for objects in the ith bin of $E(B-V)$.

Our procedure involves computing the $E(B-V)$ for each galaxy based on its rest-UV ($G - \mathcal{R}$) color, and an assumed intrinsic template and attenuation curve. The template is a combination of the Rix et al. (2004) models and the 2010 version of Starburst99 spectral synthesis models in the far-UV (Leitherer et al. 1999, 2010). The models were computed assuming a stellar metallicity of $0.28Z_\odot$, based on current solar abundances (Asplund et al. 2009), with a constant star formation history and age of 100 Myr. This particular combination of parameters was found to best reproduce the UV stellar wind lines blueward of Lyα (e.g., C III λ1176), as well as the N V λ1240 and C IV λ1549 P-Cygni profiles. The star formation history and age of the model (100 Myr) were chosen to be consistent with the results from stellar population modeling of $z \sim 3$ LBGs presented in Shapley et al. (2001) and Reddy et al. (2012). On average, such galaxies exhibit UV-to-near-IR SEDs and bolometric SFRs that are well-described by either a rising or constant star formation history (Reddy et al. 2012). For these star formation histories, the UV spectral shape remains constant for ages $\gtrsim$100 Myr as the relative contribution to the UV light from O and B stars stabilizes after

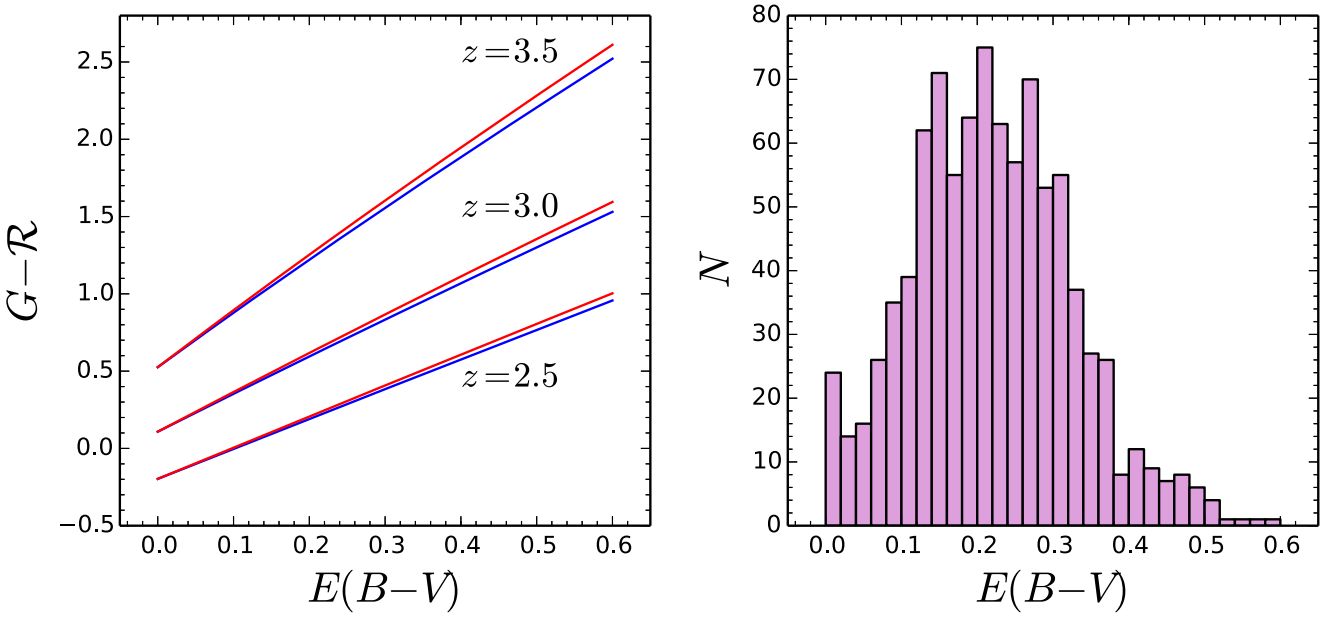

Figure 3. Left: relationship between $E(B-V)$ and $G-\mathcal{R}$ color using the intrinsic template and an IGM opacity based on the N(H I) column density distribution of Rudie et al. (2013). The relationship is shown for three redshifts, assuming either the Calzetti et al. (2000) or Reddy et al. (2015) attenuation curves, indicated by the *red* and *blue* lines, respectively. Right: distribution of $E(B-V)$ for the 933 galaxies in our sample, where the $E(B-V)$ have been computed assuming the Calzetti et al. (2000) attenuation curve.

this point. Moreover, there are no significant correlations between reddening and either star formation history or age for galaxies in our sample (Reddy et al. 2012). Thus, adopting a different model star formation history and age will serve to systematically shift the computed $E(B-V)$, but the value of the attenuation curve, which depends on the *difference* in the average $E(B-V)$ from bin-to-bin (Equation (1)), will be unaffected. Nebular continuum emission was added to the stellar template to produce a final model that we subsequently call the "intrinsic template."[7]

We generated a grid of $G-\mathcal{R}$ colors by reddening the intrinsic template assuming $E(B-V)=0.00$–0.60, with increments of $\delta E(B-V)=0.01$, and two different attenuation curves: the Calzetti et al. (2000) and Reddy et al. (2015) curves. The former curve is the most commonly used attenuation curve for high-redshift galaxies. The latter curve is our most recent determination using a sample of 224 star-forming galaxies at redshifts $z=1.36$–2.59 from the MOSFIRE Deep Evolution Field (MOSDEF; Kriek et al. 2015) survey. While lower in redshift than most of the galaxies examined here, the MOSDEF sample covers roughly the same range in stellar mass and star formation rate as the latter. The reddened templates were redshifted and attenuated by the average IGM opacity appropriate for that redshift. The average opacity was determined by randomly drawing line-of-sight absorber column densities from the distribution measured in the Keck Baryonic Structure Survey (KBSS; Rudie et al. 2013), and then taking an average over many lines of sight. As the attenuation curve depends only on the ratio of the composite spectra and the difference in their $E(B-V)$, adopting a different prescription for the IGM opacity will not affect the shape of the attenuation curve. The models were then multiplied by the G- and $\mathcal{R}$-band transmission filters to produce a model-generated $G-\mathcal{R}$ color associated with each $E(B-V)$. The relationship between $G-\mathcal{R}$ and $E(B-V)$, and the distribution of $E(B-V)$ for the 933 galaxies in our sample, which are shown in Figure 3.

We developed an iterative derivation of the attenuation curve which has seven main steps: (1) compute the $E(B-V)$ of each object in the sample; (2) bin the objects by $E(B-V)$ and construct the composite for each bin; (3) determine the average $E(B-V)$ that best fits the composite; (4) renormalize the composite to be referenced to a dust-corrected spectrum with a 1500 Å flux density equal to unity; (5) compute the $k(\lambda)$ curve from the ratio of the composite spectra in different $E(B-V)$ bins, and fit a curve to it; (6) compute the variation between the new $k(\lambda)$ and that of the previous iteration; and (7) repeat Steps (1) through (6) until the shape of the curve converges. A flowchart of the procedure is depicted in Figure 4.

Our calculation presents several advantages. First, performing this analysis using the composite spectra of many galaxies allows us to average over the stochastic variations in the Lyα forest so that the resulting composites can be used reliably to measure the far-UV shape of the dust attenuation curve. Second, as noted above, the average stellar populations of galaxies contributing to each bin of $E(B-V)$ are similar. As the far-UV portion of the spectrum is dominated by only the most massive stars, the shape of the spectrum remains constant after $\approx$100 Myr and is insensitive to the presence of older stellar populations. Third, the stellar mass distribution of $z\sim3$ LBGs in our sample, which spans the range from a few $\times10^9$ $M_\odot$ to $\approx10^{11}$ $M_\odot$, implies an $\approx$0.3 dex difference in mean oxygen abundance from the lowest to highest stellar mass galaxies in our sample based on the stellar mass–metallicity relation at z $\sim$ 3 (Troncoso et al. 2014). Assuming a similar range of stellar metallicities for a fixed star formation history and IMF implies a $\lesssim$10% difference in the intrinsic UV slope across the range of galaxies considered here. Thus, variations in

[7] The model that includes nebular continuum emission results in $E(B-V)$ that are systematically smaller (because the spectrum of the template is redder), typically by $\delta E(B-V)\simeq0.03$–0.05, than a model that includes only the stellar light.

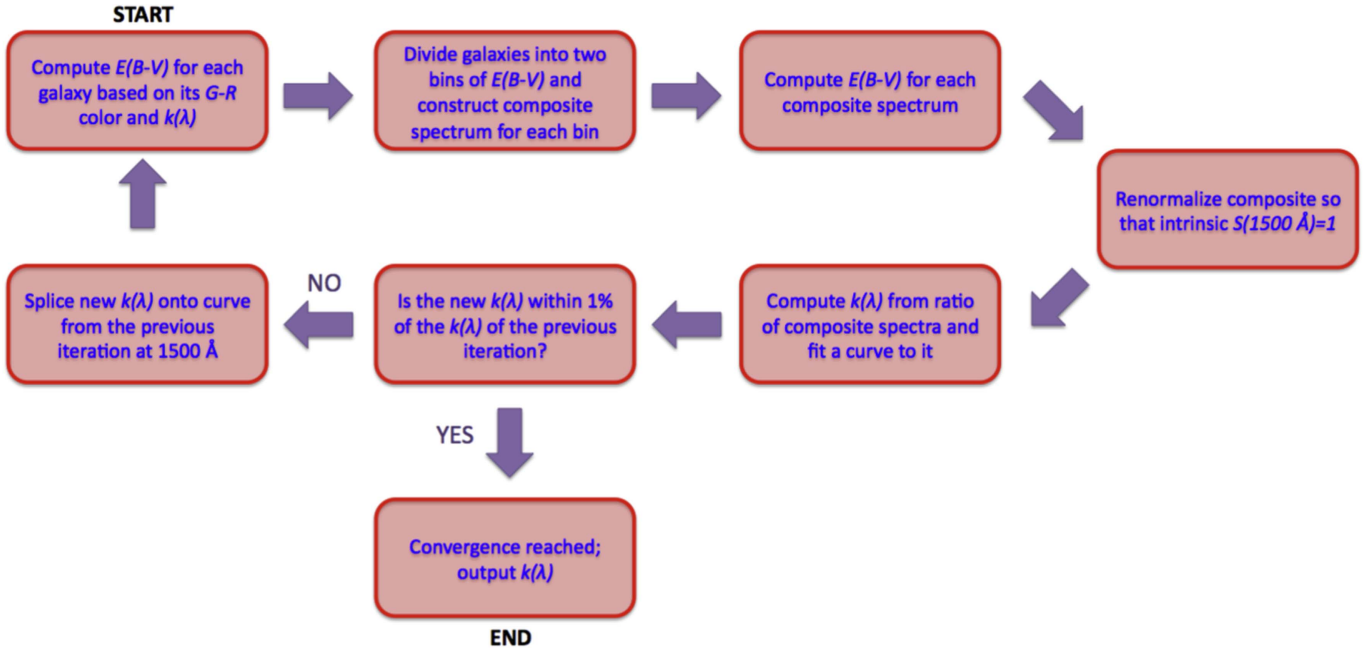

Figure 4. Flowchart of the iterative procedure used to compute the attenuation curve, $k(\lambda)$. See the text for a detailed description of each step in the derivation.

the composite spectral shapes are driven primarily by changes in dust attenuation rather than by differences in stellar metallicity. The details of our dust attenuation curve calculation are presented below.

3.1. Derivation

In Step 1, the observed $G - \mathcal{R}$ color of each galaxy was corrected for Lyα emission or absorption as measured from the rest-UV spectrum. This line-corrected color was compared to the model-generated $G - \mathcal{R}$ colors for each attenuation curve in order to find the appropriate $E(B - V)$. In Step 2, the galaxies were sorted and divided into two bins of $E(B - V)$, a "low" ("blue") and "high" ("red") $E(B - V)$ bin, with roughly an equal number of galaxies in each bin (466 and 467 objects, respectively). The composite spectrum was computed for the objects in each bin of $E(B - V)$, resulting in a "blue" and "red" $E(B - V)$ composite, following the procedure specified in Section 2.2.

For Step 3, the best-fit $E(B - V)$ for each composite spectrum was determined by taking the same intrinsic template specified above and reddening it according to the Calzetti et al. (2000) and Reddy et al. (2015) attenuation curves using the same range of $E(B - V)$ specified above. These models were then redshifted to the mean redshift of objects contributing to the composite, and attenuated according to the IGM opacity appropriate for that redshift. The model that best fits the composite spectrum then determines the $E(B - V)$. We considered the largely line-free wavelength windows listed under "Composite $E(B - V)$" in Table 1 when comparing the model spectrum to the composite. The best-fit $E(B - V)$ was found by an χ^2 minimization of the model with respect to the composite spectrum. The $E(B - V)$ computed in this way agreed well with the value inferred from the average $G - \mathcal{R}$ color of objects contributing to the composite.

In Step 4, the composite was divided by the factor $f(1500)10^{0.4E(B-V)k(1500)}$, where $f(1500)$ and $k(1500)$ are the flux density and attenuation curve, respectively, at $\lambda = 1500$ Å. This renormalization forces the dust-corrected spectrum (i.e., the spectrum obtained when de-reddening the composite according to its $E(B - V)$ for a given attenuation

Table 1
Wavelength Windows for Fitting

Type of Fitting	λ (Å)
Composite $E(B - V)$[a]	1268–1293
	1311–1330
	1337–1385
	1406–1521
	1535–1543
	1556–1602
	1617–1633
$k(\lambda)$[b]	950–970
	980–985
	994–1017
	1040–1182
	1268–1500
N(H I)[c]	967–974
	1021–1029
	1200–1203
	1222–1248
$N(H_2)$[d]	941–944
	956–960
	979–986
	992–1020

Notes.
[a] Windows used to determine the best-fit $E(B - V)$ corresponding to a composite spectrum.
[b] Windows used to determine the best polynomial fit to the far-UV shape of the attenuation curve, $k(\lambda)$.
[c] Windows used to determine the best-fit column density, N(H I), and covering fraction, f_{cov}(H I), of neutral hydrogen.
[d] Windows used to determine the best-fit column density, $N(H_2)$, and covering fraction, $f_{cov}(H_2)$, of molecular hydrogen.

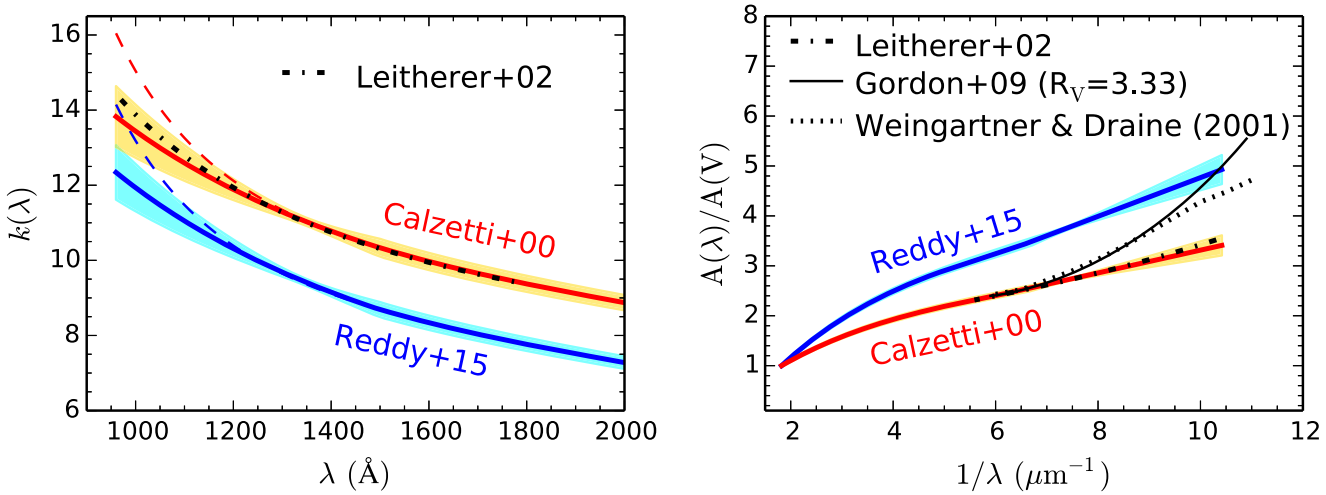

Figure 5. Left: shapes of the far-UV attenuation curves derived in this work, normalized to the Reddy et al. (2015) and Calzetti et al. (2000) attenuation curves at $\lambda = 1500$ Å (*blue* and *red* solid lines, respectively). The dashed lines indicate polynomial extrapolations of the Reddy et al. (2015) and Calzetti et al. (2000) attenuation curves based on the shapes of these curves at $\lambda \gtrsim 1200$ Å. Also shown is the far-UV attenuation curve for local galaxies from Leitherer et al. (2002). Right: $A(\lambda)/A(V)$ vs. $1/\lambda$ for the same curves shown in the left panel, where $A(\lambda)$ is the attenuation in magnitudes at wavelength λ. The average Galactic extinction curve from Gordon et al. (2009), and the model extinction curve from Weingartner & Draine (2001) are shown for comparison. The shaded regions in both panels indicate the total random error in our calculation of the far-UV attenuation curve.

curve) to have $f_{1500}^{\rm dered} = 1$. The new shape of the attenuation curve is computed in Step 5 using Equation (1). We fit the new $k(\lambda)$ with a polynomial of the form $p(\lambda) = a_0 + a_1/\lambda$, where λ is the wavelength in μm. In fitting $k(\lambda)$, we only considered windows in the far-UV ($\lambda < 1500$ Å) that are free of H I lines, and which are listed in Table 1. While the windows do include some metal lines, we confirmed by excluding the wavelength regions corresponding to the weaker interstellar and stellar absorption lines that the presence of such lines did not significantly alter the fit to the attenuation curve. In addition, we used the errors in the attenuation curve (see below) to determine the best-fit polynomial using χ^2 minimization.

In Step 6, we determined if the new $k(\lambda)$ computed in Step 5 differed from the assumed $k(\lambda)$ (i.e., the one from the previous iteration) by more than 1% at any given wavelength. If so, the new $k(\lambda)$ curve blueward of 1500 Å was spliced onto the $k(\lambda)$ from the previous iteration (note that the curve redward of 1500 Å remains fixed throughout the iterative procedure). This new version of $k(\lambda)$ was then used to repeat Steps 1 through 6. Convergence in the shape of the attenuation curve—defined such that the curve varies by no more than 1% at any wavelength from that of the previous iteration—was reached within just two or three iterations. The curves obtained when initially assuming the Reddy et al. (2015) and Calzetti et al. (2000) attenuation curves are shown in Figure 5. The best-fit polynomial to the far-UV curve with the Calzetti et al. (2000) normalization at 1500 Å, and which takes into account the random errors discussed below, is

$$k_{\rm Calz}(\lambda) = (4.126 \pm 0.345) + (0.931 \pm 0.046)/\lambda, \quad 0.095 \leqslant \lambda \leqslant 0.150\ \mu{\rm m}. \tag{2}$$

As shown in Figure 5, this polynomial is essentially identical to the fit presented in Calzetti et al. (2000) for $1250 \leqslant \lambda \leqslant 1500$ Å, but deviates from the former curve at shorter wavelengths ($\lambda < 1250$ Å). Similarly, the functional fit to the curve with the Reddy et al. (2015) normalization at 1500 Å is

$$k_{\rm Reddy}(\lambda) = (2.191 \pm 0.300) + (0.974 \pm 0.040)/\lambda, \tag{3}$$

defined over the same wavelength range specified in Equation (2).

3.2. Random and Systematic Uncertainties

There are several sources of random errors in our calculation of the far-UV attenuation curve. First are the measurement errors in the composite spectra (Section 2.2). Second are measurement uncertainties in the $G - \mathcal{R}$ colors, which can scatter galaxies from one $E(B-V)$ bin to another. Third are deviations away from the attenuation curve from one galaxy to another (e.g., due to differences in dust/stars geometries), which will affect the $E(B-V)$ inferred for a given $G - \mathcal{R}$ color. Fourth are random variations in the IGM opacity when averaged over the 466 and 467 sightlines (70 and 60 sightlines for $\lambda < 1150$ Å) that contribute to the two $E(B-V)$ bins. The combined effect of these sources of random error was quantified by calculating $k(\lambda)$ many times using the same procedure described above, where each time we (a) varied the $G - \mathcal{R}$ color of each galaxy according to its measurement uncertainty; (b) perturbed the $E(B-V)$ associated with the $G - \mathcal{R}$ color for a given attenuation curve by $\Delta E(B-V) = 0.1$ based on the intrinsic scatter of galaxies used to calibrate the Meurer et al. (1999) and Calzetti et al. (2000) relations, but ensuring that $E(B-V) \geqslant 0$; (c) randomly drew 466 and 467 sightlines (and 70 and 60 sightlines) based on the H I column density distribution measured from KBSS; and (d) perturbed the composite spectra according to the corresponding error spectra. We then computed the dispersion in the fits of the attenuation curve obtained at each wavelength from these simulations to estimate the random error in the attenuation curve. The total random error obtained in this way is indicated by the shaded regions around the attenuation curves shown in Figure 5. Note that while the random error increases toward bluer wavelengths at $\lambda \lesssim 1200$ Å, this error is still a factor $\gtrsim$3 smaller than the

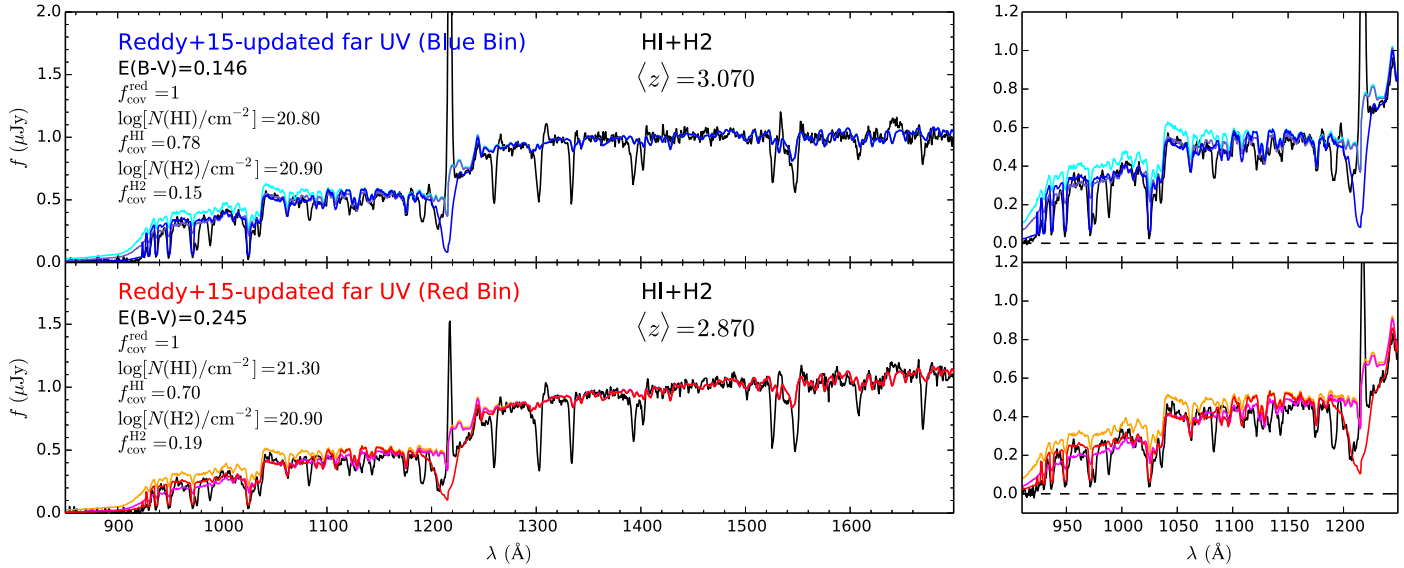

Figure 6. Best-fitting models to the composite spectra (*black*) in the blue (top) and red (bottom) bins of $E(B-V)$. The intrinsic template was modified by the IGM opacity appropriate for the mean redshift of objects contributing to the composites. The fits were then obtained in three steps. In the first, we found the value of $E(B-V)$ that minimizes the differences between the model and composite spectra in the "Composite $E(B-V)$" wavelength windows specified in Table 1, assuming the updated Reddy et al. (2015) attenuation curve and a unity covering fraction of dust $f_{\rm cov}^{\rm red}=1$ (in this first step, H I and H_2 absorption are ignored). These fits are indicated by the *cyan* and *orange* lines in the top and bottom panels, respectively. For comparison, the fits obtained assuming the original Reddy et al. (2015) attenuation curve are shown by the *dark blue* and *magenta* lines in the top and bottom panels, respectively; these fits underestimate the continuum at $\lambda<1050$ Å. In the second step we simultaneously varied the column density, N(H I), and covering fraction, $f_{\rm cov}$(H I), of neutral hydrogen until the differences between the model and composite were minimized in the "N(H I)" wavelength windows specified in Table 1. In the third and final step, we simultaneously varied the column density, $N(H_2)$, and covering fraction, $f_{\rm cov}(H_2)$, of molecular hydrogen until the differences between the model and composite were minimized in the "$N(H_2)$" wavelength windows specified in Table 1. The final fits for the $E(B-V)$ and combined H I and H_2 absorption are indicated by the solid (*blue* and *red*) lines in the top and bottom panels, respectively. For clarity, the far-UV region blueward of Lyα is shown in the right panels.

systematic differences between our new determinations of $k(\lambda)$ and the extrapolations of the original Calzetti et al. (2000) and Reddy et al. (2015) curves. Thus, the differences between the new far-UV curves derived here and the extrapolations of the original Calzetti et al. (2000) and Reddy et al. (2015) curves at $\lambda\lesssim1200$ Å are statistically significant.

The largest source of systematic error in the far-UV curve is the attenuation curve initially assumed for the calculation (Section 2.2), as demonstrated in Figure 5. The far-UV shape of $k(\lambda)$ is similar regardless of whether we have assumed the Reddy et al. (2015) or Calzetti et al. (2000) curves when initially calculating the $E(B-V)$ for galaxies in our sample, but, because of the way in which we calculate $k(\lambda)$, the normalization is fixed to that of the initially assumed attenuation curve at 1500 Å. Thus, the normalization of $k(\lambda)$ is unconstrained in our analysis.

A second source of a systematic error arises from the fact that the gas covering fractions and/or column densities of H I and H_2, as well as ISM metal absorption, might be expected to increase with $E(B-V)$. Given that we have computed the attenuation curve in the far-UV where such lines become prevalent (Figure 2), we must assess whether differences in the average absorption present in the composites for the low and high $E(B-V)$ bins have a significant impact on our calculation of $k(\lambda)$—such differences would cause us to over-estimate the value of $k(\lambda)$. This issue is addressed in Section 4.

Other sources of systematic uncertainties include our choice of the intrinsic template and the extrapolation of the H I column density distributions measured in KBSS to $z>2.8$. Both of these have a negligible effect on the derived attenuation curve as systematic changes in the intrinsic template or the extrapolation used to model the Lyα forest at $z>2.8$ will tend to systematically shift the $E(B-V)$ of individual objects either up or down, but the ordering of the galaxies in $E(B-V)$ will be preserved.

3.3. Comparison to Other Attenuation Curves

Our calculation marks the first spectroscopic direct measurement of the far-UV attenuation curve at high redshift using spectroscopic data extending to the Lyman break at 912 Å. As can be seen from Figure 5, the dust curve derived here rises less rapidly at $\lambda\lesssim1200$ Å than the polynomial extrapolations of the Reddy et al. (2015) and Calzetti et al. (2000) attenuation curves; the latter were empirically calibrated for $\lambda\gtrsim1200$ Å.

The far-UV attenuation curve derived here agrees well with that of Leitherer et al. (2002) for local star-forming galaxies. For comparison, Figure 5 also includes the Gordon et al. (2009) average extinction curve measured over 75 individual Galactic sightlines, and the extinction curve obtained from the dust grain model of Weingartner & Draine (2001). In general, the far-UV attenuation curve has a shallower dependence on wavelength than the Galactic extinction curve, though the comparison is complicated by the fact that the curve derived here is an *attenuation* curve which represents an average reddening across many sightlines. Thus the differences observed between the various curves in the far-UV may be tied to variations in the spatial geometry of the dust and stars, as well as to changes in the dust grain size distribution, and scattering and absorption cross-sections. The new far-UV measurements of the attenuation curves derived here are subsequently referred to as the "updated" versions of the Reddy et al. (2015) and Calzetti et al. (2000) curves.

4. SPECTRAL FITTING

We assessed whether the UV attenuation curve can adequately describe the composite spectra of galaxies in our sample, and, in the process, determined the magnitude of any systematic variations in the H I and H_2 column densities, and metal absorption between the two bins of $E(B-V)$ used to calculate the curve. To accomplish this, we reddened the intrinsic template by various amounts assuming the updated Reddy et al. (2015) attenuation curve and a unity covering fraction of dust ($f_{\rm cov}^{\rm red}=1$), and determined which $E(B-V)$ results in the best fit to the composite spectrum. Enforcing $f_{\rm cov}^{\rm red}=1$ was motivated by the fact that the attenuation curve is defined assuming that the entire galaxy is reddened by some average amount. The fitting was accomplished using the "Composite $E(B-V)$" windows specified in Table 1. We refer to these as the "$E(B-V)$ Only" fits (i.e., fits that do not include the H I lines or Lyman–Werner absorption from H_2), and they are shown for the two $E(B-V)$ bins in Figure 6. The uncertainty in $E(B-V)$ is $\sigma(E(B-V))\approx 0.01$ based on perturbing the composite spectra according to their errors and re-fitting them many times. While these models provide a good fit to the composite spectra at $\lambda > 1260$ Å, they clearly over-predict the observed continuum level at bluer wavelengths, which implies that additional absorption must be present at these wavelengths.

At first glance, the discrepancy between the reddened templates and the composite spectra in the far-UV may appear to be at odds with the fact that the attenuation curve was derived from the composite spectra themselves. However, recall that the attenuation curve is calculated from the *ratio* of the composite spectra. Systematic absorption in the far-UV that is present in the individual composite spectra will largely "divide out" in the calculation of the attenuation curve.

In the next iteration of the spectral fitting, we accounted for absorption by neutral hydrogen within the galaxies as follows. We added H I Lyman series absorption to the intrinsic template, assuming a Voigt profile with a Doppler parameter $b=125\,{\rm km\,s^{-1}}$ and varying column densities, $N({\rm H\,I})$. The wings of the line profile are insensitive to the particular choice of b. We also blueshifted the H I absorption lines relative to the model by $300\,{\rm km\,s^{-1}}$ to provide the best match to the observed wavelengths of the lines in the composite. This blueshift is generally attributed to galactic-scale outflows of gas seen in absorption against the background stellar continuum. The composite spectra were compared to the model spectra, where the latter were computed as:

$$m_{\rm final}=10^{-0.4E(B-V)k}\times[f_{\rm cov}({\rm H\,I})m({\rm H\,I})+(1-f_{\rm cov}({\rm H\,I}))m], \quad (4)$$

where $f_{\rm cov}({\rm H\,I})$ is the covering fraction of neutral hydrogen; $m({\rm H\,I})$ and m are the intrinsic templates with and without H I absorption, respectively; and $E(B-V)$ is the value found above (from the $E(B-V)$ Only fitting). Note that the reddening was applied to the entire spectrum; i.e., $f_{\rm cov}^{\rm red}=1$. These final models were computed for a range of $N({\rm H\,I})$ and $f_{\rm cov}({\rm H\,I})$, and modified by the IGM opacity appropriate for the average redshift of each composite.

The final models were compared to the composite spectra in the "$N({\rm H\,I})$" wavelength windows specified in Table 1 to find the best-fitting combination of $N({\rm H\,I})$ and $f_{\rm cov}({\rm H\,I})$. The wavelength windows were chosen to avoid regions of strong metal line absorption (e.g., C III λ977 and C II λ1036) and strong Lyα emission, and include the core and as much of the wings of Lyβ and Lyγ, and the wings of Lyα, particularly the region between Lyα and N V λ1238. The higher Lyman series lines (Lyδ and greater) were not used due to the larger random errors at these wavelengths and because these lines begin to overlap. The covering fraction is constrained primarily by the depths of the lines, whereas the column density is most sensitive to the wings. The fitting suggests column densities of $\log[N({\rm H\,I})/{\rm cm^{-2}}]\approx 20.8$–$21.3$ and covering fractions of $f_{\rm cov}({\rm H\,I})\approx 0.70$–$0.78$ for the two bins of $E(B-V)$ (Figure 6). By perturbing the composite spectra and re-fitting the data many times, we estimated the (measurement) errors in $\log[N({\rm H\,I})/{\rm cm^{-2}}]$ and $f_{\rm cov}({\rm H\,I})$ to be $\sigma(\log[N({\rm H\,I})/{\rm cm^{-2}}])\approx 0.20$ dex and $\sigma(f_{\rm cov}({\rm H\,I}))\approx 0.01$, respectively. The systematic error in $\log[N({\rm H\,I})/{\rm cm^{-2}}]$ from changing the Doppler parameter by a factor of two from our assumed value is $\sigma(\log[N({\rm H\,I})/{\rm cm^{-2}}])\approx 0.10$ dex.

Note that the values of $f_{\rm cov}({\rm H\,I})$ derived here are physically meaningful only if the H I lines are optically thick *and* the residual flux observed at the H I line cores is not an artifact of limited spectral resolution, redshift imprecision, or foreground contamination. In the first case, a high $N({\rm H\,I})$ is required to reproduce the damping wings of Lyα, Lyβ, and Lyγ, implying optically thick gas. In the second case, as shown in detail in Reddy et al. (2016), redshift and spectral resolution uncertainties are not sufficient to account for the residual flux seen at the H I line centers. Briefly, we executed simulations where we added H I of varying column densities to the intrinsic spectrum, replicated many versions of this H I-absorbed spectrum with slightly different redshifts based on the typical redshift uncertainty for galaxies in our sample, smoothed these versions with various values of the spectral resolution, and then produced a composite of all these versions. This exercise revealed that we would have had to systematically underestimate the rest-frame spectral resolution by more than 50% in order to reproduce the amount of residual flux at the H I line centers. This 50% is much larger than the rms uncertainties in determining the spectral resolution from the widths of night sky lines. Lastly, we ruled out foreground contamination as a source of the residual flux based on the exclusion of spectroscopic blends from our sample and the fact that this flux inversely correlates with reddening, a result that would not be expected if the flux was dominated by foreground contaminants (see Reddy et al. 2016 for more discussion). Thus, we conclude that the spectra can be modeled with a partial covering fraction of optically thick H I.

In the final iteration of the fitting, we included H_2 Lyman–Werner absorption in the models as follows:

$$m_{\rm final}=10^{-0.4E(B-V)k}\times[(f_{\rm cov}({\rm H\,I})-f_{\rm cov}({\rm H_2}))m({\rm H\,I})+f_{\rm cov}({\rm H_2})m({\rm H\,I}+{\rm H_2})+(1-f_{\rm cov}({\rm H\,I}))m], \quad (5)$$

where $f_{\rm cov}({\rm H_2})$ is the covering fraction of molecular hydrogen, $m({\rm H\,I}+{\rm H_2})$ is the model including both H I and H_2 absorption, and the remaining variables have the same definitions as in Equation (4). This calculation assumes that the H_2 is entirely embedded in H I clouds.

H_2 absorption was modeled using the McCandliss (2003) templates, assuming a Doppler parameter $b\sim 20\,{\rm km\,s^{-1}}$, all vibrational transitions from the first vibrational mode, and the

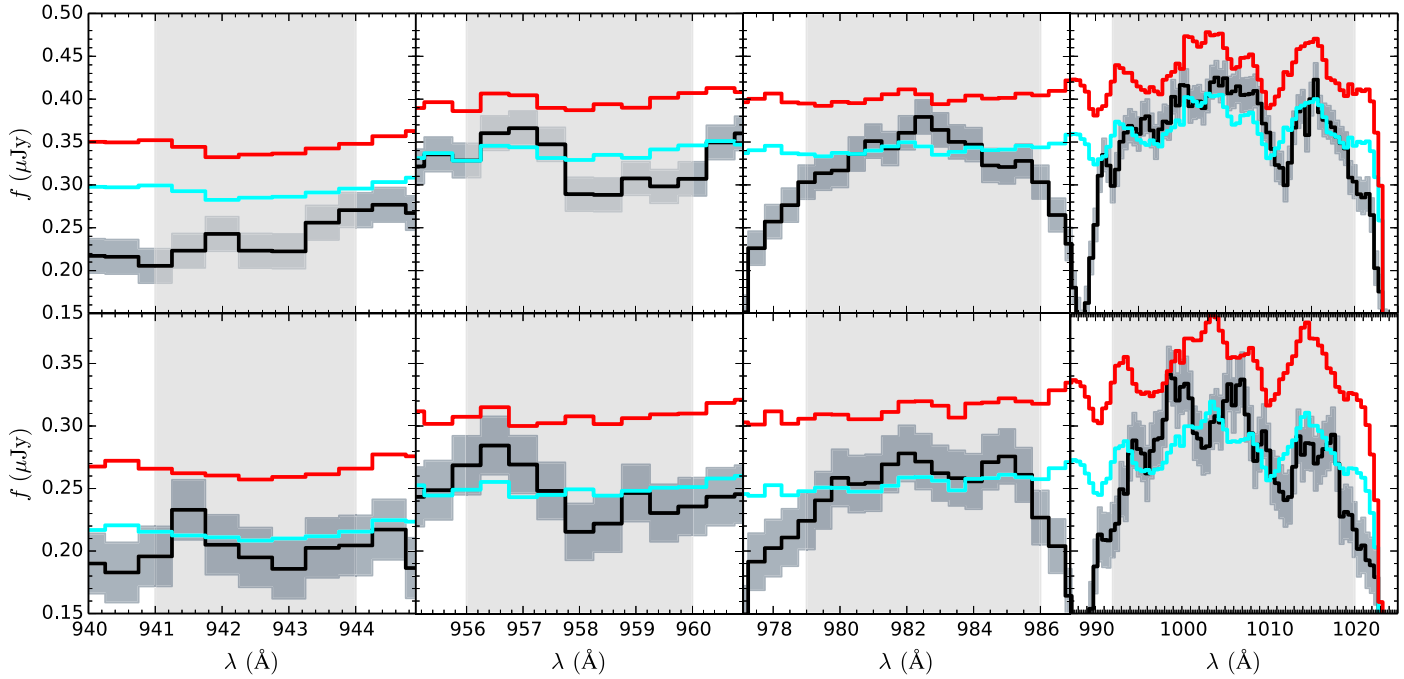

Figure 7. Comparison between the composite spectrum (*black lines*) and the best-fit models with (*cyan*) and without (*red*) fitting for H_2 absorption in the four "$N(H_2)$" windows specified in Table 1. The wavelength windows are indicated by the light shaded regions. The top and bottom rows show the comparison for the composite spectra in the blue and red bins of $E(B-V)$, respectively. In general, the fits that include H_2 absorption are in better agreement with the composite spectra than the fits that exclude this absorption. For reference, the $\pm1\sigma$ uncertainty in the composite fluxes are denoted by the dark shaded regions.

$J = 1$–6 transitions. The templates were smoothed to match the resolution of the composite spectra. In fitting the models to the composite spectra, the $E(B-V)$, $N(\mathrm{H\,I})$, and $f_{\rm cov}(\mathrm{H\,I})$ were fixed to the values found above, and $N(H_2)$ and $f_{\rm cov}(H_2)$ were allowed to vary. The "best-fit" $N(H_2)$ and $f_{\rm cov}(H_2)$ were found by minimizing the differences in the model and composite spectra in the four wavelength windows indicated by the "$N(H_2)$" entry in Table 1. These windows were chosen because they are free from H I absorption and strong metal line absorption as identified in the Far Ultraviolet Spectroscopic Explorer (FUSE) spectra of the LMC by Walborn et al. (2002). The best-fitting models including H_2 are shown in Figure 6, and we find $f_{\rm cov}(H_2) \approx 0.15$–$0.19$ and $\log[N(H_2)/\mathrm{cm}^{-2}] \approx 20.9$. As the H_2 lines are blended and unresolved, we cannot accurately determine the errors in the fitted parameters. Nevertheless, we note that the deficit in the flux of the composites relative to the models which *do not* include the Lyman–Werner bands in the four H_2 windows (Table 1) implies that H_2 absorption must be present, albeit with a low covering fraction or low column density (Figure 7).[8] The apparently low covering fraction of H_2 relative to that of the H I and dust implies that most of the dust in the ISM of typical galaxies at $z \sim 3$ is unrelated to the catalysis of H_2 molecules, and is associated with other phases of the ISM (e.g., ionized and neutral gas). This result is robust against the assumption of a non-unity covering fraction of dust. In other words, as shown in Reddy et al. (2016b), assuming a *partial* covering fraction of dust yields dust covering fractions that are $\gtrsim$92%, still much larger than the covering fraction deduced for H_2.

The aforementioned fitting demonstrates that the updated Reddy et al. (2015) curve provides a reasonable fit to the composite spectra over the entire far-UV through near-UV range once H I and H_2 absorption are accounted for. We found similar results when considering the updated Calzetti et al. (2000) attenuation curve. Moreover, the column density and covering fraction of H_2 indicate a similar degree of absorption of the far-UV continuum between the blue and red $E(B-V)$ bins, implying that systematic differences in this absorption are negligible and thus unlikely to bias our estimate of the far-UV shape of the dust attenuation curve. In comparison, the original versions of these dust curves imply a far-UV rise that is too steep to simultaneously model the mid-UV range used to compute $E(B-V)$ ($\lambda = 1268$–1633 Å) and the far-UV at $\lambda \lesssim 1050$ Å (Figure 6).

5. DISCUSSION

A primary result of our analysis is that the far-UV attenuation curve rises less rapidly toward bluer wavelengths ($\lambda \lesssim 1250$ Å) relative to other commonly assumed attenuation curves. A consequence of this less-rapid far-UV rise is a lower attenuation of LyC photons by dust. In particular, the average $E(B-V)$ for galaxies in our $z \sim 3$ sample is $\langle E(B-V)\rangle_{\rm Calz} = 0.20$ and $\langle E(B-V)\rangle_{\rm MOS} = 0.21$ if we assume the Calzetti et al. (2000) and Reddy et al. (2015) reddening curves, respectively. For these values, the attenuation of LyC photons at $\lambda = 900$ Å is a factor of $\approx$1.8–2.3 lower than that inferred using polynomial extrapolations of the Calzetti et al. (2000) and Reddy et al. (2015) curves at $\lambda < 1200$ Å. Clearly this result has implications for the fraction of hydrogen-ionizing photons that escape galaxies

[8] The absorption arising from transitions between vibrational states above the ground vibrational state of H_2 is expected to be weak relative to the absorption arising from transitions from the ground vibrational state for the typical conditions in the ISM. Transitions from the ground vibrational state (for the six rotational transitions considered here, $J = 6$–1) completely blanket the far-UV continuum, given the resolution of our spectra. Thus, adding absorption corresponding to upper level vibrational transitions will simply remove "power" from the considered (ground state vibrational) mode, and the column densities and covering fractions derived here would be upper limits.

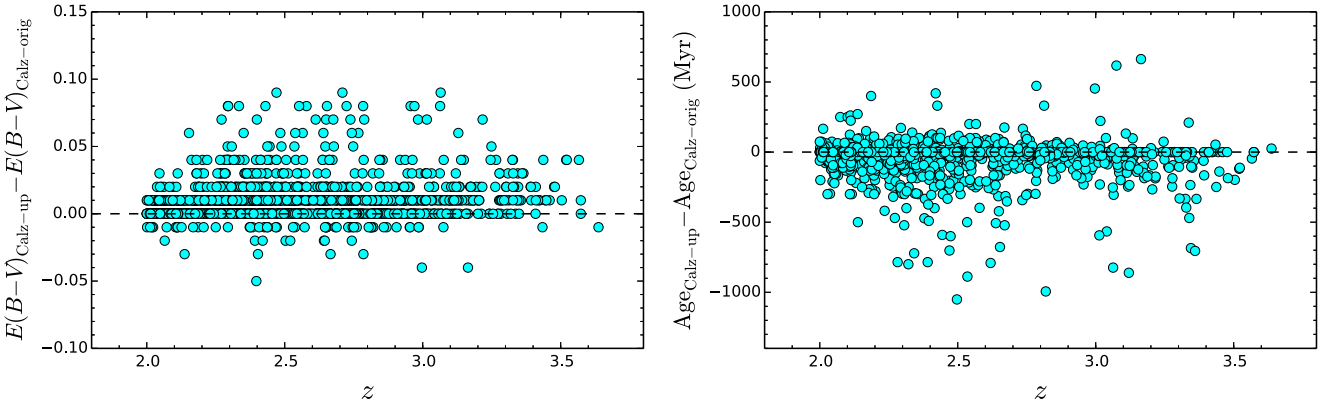

Figure 8. Difference in the $E(B-V)$ and ages derived from stellar population modeling for 1874 KBSS galaxies when assuming the updated and original forms of the Calzetti et al. (2000) attenuation curve. The updated form of the curve, which incorporates the new shape of the far-UV curve derived here, results in $E(B-V)$ and ages that are on average ≈0.008 mag redder and 50 Myr younger, respectively, than those derived assuming the original Calzetti et al. (2000) curve.

before being absorbed by hydrogen in the IGM or CGM, i.e., the ionizing escape fraction. At face value this result implies a larger escape fraction of ionizing photons for galaxies of a given dust reddening. However, as discussed in Reddy et al. (2016b), the actual covering fraction of neutral gas likely plays a larger role in modulating the escape of such photons than attenuation by dust. Specifically, the dominant mode by which ionizing photons escape L^* galaxies at $z\sim3$ is through channels that have been cleared of gas and dust, while other sightlines are characterized by optically thick H I that extinguishes ionizing photons through photoelectric absorption (Reddy et al. 2016b). Regardless, our new determinations of the far-UV dust curve have direct applications to assessing the attenuation of ionizing photons either internal to H II regions (e.g., Petrosian et al. 1972; Natta & Panagia 1976; Shields & Kennicutt 1995; Inoue 2001; Dopita et al. 2003) or—in the context of high-redshift galaxies—in the ionized galactic-scale ISM, or in low column density neutral gas (i.e., $\log[N({\rm H\,I})/{\rm cm^{-2}}]\lesssim17.2$) where dust absorption begins to dominate the depletion of ionizing photons.

The revised shape of the far-UV curve also has consequences for the reddening and ages of galaxies derived from stellar population (i.e., SED) modeling. To illustrate this, we considered 1874 galaxies from KBSS that have ground-based $U_{\rm n}G\mathcal{R}$, near-IR intermediate-band ($J2$, $J3$, $H1$, $H2$), and broad-band (J, $K_{\rm s}$) photometry, along with *Hubble Space Telescope* WFC3/IR F160W and *Spitzer Space Telescope* IRAC imaging (Strom et al. 2016). We fit Bruzual & Charlot (2003) $0.2Z_\odot$ stellar population models to the photometry, assuming a constant star formation history, $E(B-V)$ in the range 0.0–0.6, and ages from 50 Myr to the age of the universe at the redshift of each galaxy (a full description of the SED-fitting procedure is provided in Reddy et al. 2012). The modeling was performed assuming the original form of the Calzetti et al. (2000) attenuation curve as well as the updated version (i.e., which incorporates the new shape of the far-UV curve found here). Figure 8 shows the comparison between the reddening and ages derived for galaxies in KBSS as a function of redshift for the two versions of the attenuation curve. A less rapid rise of the far-UV attenuation curve implies that a larger reddening is required to reproduce the rest-UV color, which in turn makes the galaxies appear younger. Thus, the updated attenuation curve results in $E(B-V)$ that are on average ≈0.008 mag redder and ages that are on average ≈50 Myr younger than those derived with the original Calzetti et al. (2000) curve. The redder $E(B-V)$ result in SFRs that are about 8% larger, while the stellar masses do not change appreciably. Of course, the magnitude of the effect of changing the far-UV attenuation curve on the derived stellar population parameters depends on which bands are being fit. For galaxies at $z\sim2$–3, where the Lyα forest is thin and the $U_{\rm n}$ and G-bands probe the rest-frame far-UV, we find systematic offsets in both the reddening and ages of galaxies.

6. SUMMARY

To summarize, we have used a large sample of 933 spectroscopically confirmed $\mathcal{R}<25.5$ LBGs at $z\sim3$, 121 of which have very deep spectroscopic coverage in the range $850\lesssim\lambda\lesssim1300$ Å, in order to deduce the shape of the far-UV ($\lambda=950$–1500 Å) dust attenuation curve. We used an iterative procedure to construct composite spectra of the $z\sim3$ LBGs in bins of continuum color excess, $E(B-V)$, and, by taking ratios of these spectra, we calculated the far-UV wavelength dependence of the dust attenuation curve.

The curve found here implies a lower attenuation at $\lambda\lesssim1250$ Å relative to that inferred from simple polynomial extrapolations of the Calzetti et al. (2000) and Reddy et al. (2015) attenuation curves. Our new determination of the far-UV shape of the dust curve enables more accurate estimates of the effect of dust on the attenuation of hydrogen-ionizing (LyC) photons. Specifically, our results imply a factor of ≈2 lower attenuation of LyC photons for typical $E(B-V)$ relative to that deduced from simple extrapolations of the most widely used attenuation curves at high redshift. Our results may be used to assess the degree of LyC attenuation internal to H II regions, in the ionized media of high-redshift galaxies, or in low column density ISM ($\log[N({\rm H\,I})/{\rm cm^{-2}}]\lesssim17.2$).

The composite spectra of $z\sim3$ galaxies can be described well by a model that assumes our new attenuation curve with a unity covering fraction of dust, an ≈70%–80% covering fraction of H I, and additional absorption associated with the Lyman–Werner bands of H_2. The inferred covering fraction of H_2 is very low ($\lesssim$20%) and, when contrasted with the high covering fraction of dust, suggests that most of the dust in the ISM of high-redshift galaxies is not associated with the catalysis of H_2. The dust is likely associated with other phases of the ISM, such as the ionized and/or neutral H I components.

N.A.R. is supported by an Alfred P. Sloan Research Fellowship, and acknowledges the visitors program at the Institute of Astronomy in Cambridge, UK, where part of this research was conducted. C.C.S. acknowledges NSF grants AST-0908805 and AST-1313472. M.B. acknowledges support of the Serbian MESTD through grant ON176021. We thank Allison Strom for providing the photometry for the KBSS galaxies. We are grateful to the anonymous referee whose comments led to significant improvements in the presentation of the analysis. We wish to extend special thanks to those of Hawaiian ancestry on whose sacred mountain we are privileged to be guests. Without their generous hospitality, the observations presented herein would not have been possible.

REFERENCES

Adelberger, K. L., Steidel, C. C., Shapley, A. E., et al. 2004, ApJ, 607, 226
Asplund, M., Grevesse, N., Sauval, A. J., & Scott, P. 2009, ARA&A, 47, 481
Atek, H., Kunth, D., Schaerer, D., et al. 2014, A&A, 561, A89
Brott, I., de Mink, S. E., Cantiello, M., et al. 2011, A&A, 530, A115
Bruzual, G., & Charlot, S. 2003, MNRAS, 344, 1000
Buat, V., Giovannoli, E., Heinis, S., et al. 2011, A&A, 533, A93
Buat, V., Noll, S., Burgarella, D., et al. 2012, A&A, 545, A141
Calzetti, D., Armus, L., Bohlin, R. C., et al. 2000, ApJ, 533, 682
Calzetti, D., & Kinney, A. L. 1992, ApJL, 399, L39
Calzetti, D., Kinney, A. L., & Storchi-Bergmann, T. 1994, ApJ, 429, 582
Charlot, S., & Fall, S. M. 1993, ApJ, 415, 580
Dopita, M. A., Groves, B. A., Sutherland, R. S., & Kewley, L. J. 2003, ApJ, 583, 727
Eldridge, J. J., & Stanway, E. R. 2009, MNRAS, 400, 1019
Finkelstein, S. L., Cohen, S. H., Moustakas, J., et al. 2011, ApJ, 733, 117
Giavalisco, M., Koratkar, A., & Calzetti, D. 1996, ApJ, 466, 831
Gordon, K. D., Cartledge, S., & Clayton, G. C. 2009, ApJ, 705, 1320
Hayes, M., Schaerer, D., Östlin, G., et al. 2011, ApJ, 730, 8
Inoue, A. K. 2001, AJ, 122, 1788
Johnson, B. D., Schiminovich, D., Seibert, M., et al. 2007, ApJS, 173, 377
Kriek, M., & Conroy, C. 2013, ApJL, 775, L16
Kriek, M., Shapley, A. E., Reddy, N. A., et al. 2015, ApJS, 218, 15
Leitherer, C., Ekström, S., Meynet, G., et al. 2014, ApJS, 212, 14
Leitherer, C., Li, I.-H., Calzetti, D., & Heckman, T. M. 2002, ApJS, 140, 303
Leitherer, C., Ortiz Otálvaro, P. A., Bresolin, F., et al. 2010, ApJS, 189, 309
Leitherer, C., Schaerer, D., Goldader, J. D., et al. 1999, ApJS, 123, 3
Levesque, E. M., Leitherer, C., Ekstrom, S., Meynet, G., & Schaerer, D. 2012, ApJ, 751, 67
McCandliss, S. R. 2003, PASP, 115, 651
Meier, D. L., & Terlevich, R. 1981, ApJL, 246, L109
Meurer, G. R., Heckman, T. M., & Calzetti, D. 1999, ApJ, 521, 64
Natta, A., & Panagia, N. 1976, A&A, 50, 191
Noll, S., Pierini, D., Cimatti, A., et al. 2009, A&A, 499, 69
Oke, J. B., Cohen, J. G., Carr, M., et al. 1995, PASP, 107, 375
Petrosian, V., Silk, J., & Field, G. B. 1972, ApJL, 177, L69
Reddy, N. A., Kriek, M., Shapley, A. E., et al. 2015, ApJ, 806, 259
Reddy, N. A., Pettini, M., Steidel, C. C., et al. 2012, ApJ, 754, 25
Reddy, N. A., Steidel, C. C., Erb, D. K., Shapley, A. E., & Pettini, M. 2006, ApJ, 653, 1004
Reddy, N. A., Steidel, C. C., Pettini, M., et al. 2008, ApJS, 175, 48
Reddy, N. A., Steidel, C. C., Pettini, M., et al. 2016, ApJ, 828, 109
Rix, S. A., Pettini, M., Leitherer, C., et al. 2004, ApJ, 615, 98
Rudie, G. C., Steidel, C. C., Shapley, A. E., & Pettini, M. 2013, ApJ, 769, 146
Salmon, B., Papovich, C., Long, J., et al. 2016, ApJ, 827, 20
Sawicki, M., & Thompson, D. 2006, ApJ, 642, 653
Scarlata, C., Colbert, J., Teplitz, H. I., et al. 2009, ApJL, 704, L98
Scoville, N., Faisst, A., Capak, P., et al. 2015, ApJ, 800, 108
Shapley, A. E., Reddy, N. A., Kriek, M., et al. 2015, ApJ, 801, 88
Shapley, A. E., Steidel, C. C., Adelberger, K. L., et al. 2001, ApJ, 562, 95
Shields, J. C., & Kennicutt, R. C., Jr. 1995, ApJ, 454, 807
Steidel, C. C., Adelberger, K. L., Shapley, A. E., et al. 2003, ApJ, 592, 728
Steidel, C. C., Erb, D. K., Shapley, A. E., et al. 2010, ApJ, 717, 289
Steidel, C. C., & Hamilton, D. 1993, AJ, 105, 2017
Steidel, C. C., Rudie, G. C., Strom, A. L., et al. 2014, ApJ, 795, 165
Steidel, C. C., Shapley, A. E., Pettini, M., et al. 2004, ApJ, 604, 534
Strom, A. L., Steidel, C. C., Gwen, C. R., et al. 2016, arXiv:1608.02587
Troncoso, P., Maiolino, R., Sommariva, V., et al. 2014, A&A, 563, A58
Verhamme, A., Schaerer, D., Atek, H., & Tapken, C. 2008, A&A, 491, 89
Walborn, N. R., Fullerton, A. W., Crowther, P. A., et al. 2002, ApJS, 141, 443
Weingartner, J. C., & Draine, B. T. 2001, ApJ, 548, 296
Wild, V., Charlot, S., Brinchmann, J., et al. 2011, MNRAS, 417, 1760
Zeimann, G. R., Ciardullo, R., Gronwall, C., et al. 2015, ApJ, 814, 162